High spatiotemporal resolution measurement of regional lung air volumes from 2D phase contrast x-ray images

Andrew F. T. Leong[a)]
School of Physics, Monash University, Victoria 3800, Australia

Andreas Fouras
Division of Biological Engineering, Monash University, Victoria 3800, Australia

M. Sirajul Islam
School of Physics, Monash University, Victoria 3800, Australia

Megan J. Wallace and Stuart B. Hooper
The Ritchie Centre and Department of Obstetrics and Gynaecology, Monash Institute of Medical Research, Monash University, Victoria 3168, Australia

Marcus J. Kitchen
School of Physics, Monash University, Victoria 3800, Australia

(Received 27 November 2012; revised 11 February 2013; accepted for publication 24 February 2013; published 19 March 2013)

Purpose: Described herein is a new technique for measuring regional lung air volumes from two-dimensional propagation-based phase contrast x-ray (PBI) images at very high spatial and temporal resolution. Phase contrast dramatically increases lung visibility and the outlined volumetric reconstruction technique quantifies dynamic changes in respiratory function. These methods can be used for assessing pulmonary disease and injury and for optimizing mechanical ventilation techniques for preterm infants using animal models.
Methods: The volumetric reconstruction combines the algorithms of temporal subtraction and single image phase retrieval (SIPR) to isolate the image of the lungs from the thoracic cage in order to measure regional lung air volumes. The SIPR algorithm was used to recover the change in projected thickness of the lungs on a pixel-by-pixel basis (pixel dimensions $\sim$16.2 μm). The technique has been validated using numerical simulation and compared results of measuring regional lung air volumes with and without the use of temporal subtraction for removing the thoracic cage. To test this approach, a series of PBI images of newborn rabbit pups mechanically ventilated at different frequencies was employed.
Results: Regional lung air volumes measured from PBI images of newborn rabbit pups showed on average an improvement of at least 20% in 16% of pixels within the lungs in comparison to that measured without the use of temporal subtraction. The majority of pixels that showed an improvement was found to be in regions occupied by bone. Applying the volumetric technique to sequences of PBI images of newborn rabbit pups, it is shown that lung aeration at birth can be highly heterogeneous.
Conclusions: This paper presents an image segmentation technique based on temporal subtraction that has successfully been used to isolate the lungs from PBI chest images, allowing the change in lung air volume to be measured over regions as small as the pixel size. Using this technique, it is possible to measure changes in regional lung volume at high spatial and temporal resolution during breathing at much lower x-ray dose than would be required using computed tomography.
 [http://dx.doi.org/10.1118/1.4794926]

Key words: phase contrast x-ray imaging, regional lung volume, image registration, thoracic cage segmentation, temporal subtraction

I. INTRODUCTION

Dynamic changes in regional lung air volumes and their derivatives (e.g., regional lung air flow and time constant) are key measures of regional lung mechanics and may indicate localized regions of disease well before the pathogenic changes are sufficient to cause global changes in lung function.[1] Consequently, many techniques have been developed to analyze regional lung volumes using various types of tomography-based imaging modalities (see, e.g., Refs. 2–4). Although these modalities provide regional lung volume measures, they are limited by a low temporal or spatial resolution or may require a large radiation dose for dynamic studies. We have previously developed a technique to measure regional changes in lung air volume between a pair of two-dimensional (2D) images recorded using propagation-based phase contrast x-ray imaging (PBI).[5] PBI (explained in more detail in Sec. I.B) produces phase-induced intensity variations between the boundary of materials exhibiting different refractive indices. The lung is ideal for PBI as it consists of conducting

airways and tiny air-filled alveoli that are surrounded by thin regions of tissue. The changes in refractive indices, between air and tissue, experienced by the x-ray as it traverses the lung either highlights single airways in projection or produces a speckle pattern when the x-ray passes through multiple airways[6] (see Sec. III). Combined with our phase retrieval analysis technique,[5] these images can simultaneously provide both higher order structural (i.e., alveolar regions seen as lung speckle) and regional volumetric information in real-time from 2D images. This approach avoids the use of a contrast agent, which is required in other volumetric techniques, to quantify lung volume.[2,4,7]

The presence and differential movement of the thoracic cage in relation to the lung during breathing limits the accuracy of the regional lung air volumes measured using our phase retrieval analysis.[5] As a result, our aim was to develop an algorithm to segment the ribs from PBI images of the chest before applying our analysis to measure changes in regional lung air volume. Segmentation of bones from chest images is a common radiography processing tool for isolating the lung to improve the detection of diseases. Techniques that are commonly employed include artificial neural networks (ANN), dual-energy subtraction (DES), and temporal subtraction (TS). DES involves imaging at two different x-ray energies to separate two materials by exploiting the difference in their energy-dependent attenuation coefficients and performing a weighted logarithmic subtraction.[8] This technique can be highly accurate in removing bone when the images are simultaneously recorded at two different x-ray energies.[9,10] TS facilitates visualization of pathological changes by subtracting an image from one previously captured, following alignment of the images. This has commonly been used to improve the visibility of lung lesions within chest radiographs, which has helped improve the sensitivity and specificity of lung tumor detection and monitoring.[11] Unlike DES, alignment of the images is required to correct for differential movement of the thoracic cage, which will likely introducing bone artifacts into the subtracted image. ANN can be trained to remove bone and once optimized can be easily utilized clinically, but the initial training of the network can be arduous. DES images have been used to train the network, but the ANN can, therefore, only at most be equally and not more accurate than DES.[12]

Carnibella, Fouras, and Kitchen[10] recently developed a single exposure DES technique using synchrotron radiation. Despite the images being recorded at finite distances between object and detector, the algorithm formulated assumes they are purely absorption-based images. If this technique was applied to measuring regional lung air volume, the prevalent phase-induced intensity variation in the lungs could lead to large errors. TS and ANN have yet not been developed for removal of bone from PBI images. Hence, in this paper we describe a novel TS-based algorithm to remove the bones from PBI chest images by first aligning the bones, then applying our phase retrieval analysis to remove the phase-induced intensity variations followed by subtraction of the images. This enabled us to measure changes in regional lung air volumes with much greater spatial resolution than previously possible. In Sec. I.A, we introduce our approach to phase contrast TS and briefly describe our lung volume analysis technique in Sec. I.C. A description of the algorithm and its implementation follows in Sec. II. In Sec. III, we evaluate the accuracy and robustness of the TS algorithm by examining the subtracted images and calculated lung air volumes. Some directions for future work are provided in Sec. IV and we conclude with Sec. V.

I.A. Temporal subtraction

Temporal subtraction of chest images require careful image alignment, or registration, to correct for movement of the thoracic cage during breathing and shifting of subject pose. Medical image registration is a well-established field with an exhaustive range of techniques, each with their own proponents, but they essentially follow a common framework. The process of aligning two images involves: (i) selecting and matching salient (control) points between the images and (ii) applying a transformation function to establish a point-by-point correspondence between them. Early work on TS by Kano *et al.*[13] developed a nonrigid area-based registration algorithm and showed it improved the discernibility of metastatic lung nodules in radiographs. This prompted the development of other registration techniques that have improved upon the accuracy and robustness against more elaborate chest movements. An excellent review on similarity measures and interpolation functions applied in medical image registration is provided by Zitová and Flusser.[14]

Here, we employ the standard approach of Kano *et al.*[13] for the purposes of measuring regional lung air volume using 2D PBI images by adapting the cross correlation (CC) similarity measure to locally match regions-of-interest (ROIs) between two images, denoted A and B. The CC can be computed efficiently using fast Fourier transforms via the relation

$$CC = \mathbf{F}^{-1}[\mathbf{F}\{\bar{a}\} \times \mathbf{F}^{*}\{\bar{b}\}], \tag{1}$$

where $\bar{a}$ and $\bar{b}$ are the mean subtracted ROI from image A (kernel) and the ROI from image B (search area), respectively, while $\mathbf{F}$ and $\mathbf{F}^{-1}$ are the Fourier and inverse Fourier transform pairs, respectively. $\mathbf{F}^{*}\{\bar{b}\}$ is the complex conjugate of $\mathbf{F}\{\bar{b}\}$.

Ideally, the peak in each CC matrix describes the representative translation vector for each ROI pair. In x-ray imaging of the chest however, multiple peaks often appear due to the repetitive structure of the ribs in the chest. Consequently, the kernel and search area are selected in close vicinity of one another and their sizes are carefully chosen. The endpoints of each representative translation vector are defined as a pair of control points (i), $(x_{A,i}, y_{A,i}) \subseteq A$ and $(x_{B,i}, y_{B,i}) \subseteq B$. CC has been employed in a wide variety of medical imaging research including the study of lung motion and blood flow, which can potentially be used for early diseases detection and with greater precision.[15,16]

To apply a transformation matrix on image A to align with image B we employ Delaunay triangulation. It returns a highly accurate interpolation as the total distance between control points from which coordinates are interpolated is minimized.[17]

The main problem with image registration is that radiographs are 2D projections of three-dimensional (3D) objects. This complicates the alignment as structures moving independently of one another in 3D may be overlaid in the projected image, thereby limiting the accuracy of the registration. A chest encompasses several independently moving parts including the ribs, heart, and lungs. Thus, most registration techniques are restricted to correcting for small movements in the projected plane.

Evaluating the registration accuracy is not straightforward as there is often no gold standard that exemplifies perfect alignment. Most registration evaluation is done by visually inspecting for artifacts present in the subtracted image and/or by computing multiple metrics such as the squared intensity error and reverse consistency error.[18]

I.B. Phase contrast x-ray imaging

Conventional x-ray imaging struggles to differentiate between soft biological tissues without the use of contrast agents.[19] Phase contrast x-ray imaging (PCXI) is able to enhance the boundaries of soft tissue by exploiting the differences in their refractive indices.[20] Many PCXI techniques have been developed that are suitable for biomedical studies, namely, PBI, analyzer-based phase contrast x-ray imaging and grating interferometry.[21] The improved contrast can be traded against a reduction in x-ray dose. Also, since the real part of the complex refractive index decreases with increasing x-ray energy at a much slower rate than the imaginary (absorptive) part, the dose can be decreased by employing higher x-ray energy.[21] Currently, PCXI is predominantly done using synchrotron radiation as it requires sufficient spatial coherence to induce edge enhancements. Despite this, there has been much success in performing PCXI imaging using laboratory-based x-ray sources.[22,23] PBI allows a simple setup as it does not require any postobject optics. Essentially, a spatially coherent source and a sufficient object-to-detector propagation distance are all that is required. The nonzero object-to-detector propagation distance enables refracted rays to produce interference/diffraction fringes.

I.C. Lung air volume analysis

Our work builds on that of Kitchen *et al.*[5] to determine the change in regional lung air volume between a pair of 2D PBI images for studying rapid changes in lung aeration. There the subject's thorax was immersed in a container of water and positioned between a partially coherent x-ray synchrotron source and detector. The change in the volume of air inside the lungs was equal to that of the water displaced from the main (sealed) chamber into the attached reservoir (water column; see Fig. 1). Determining the displaced water volume can be achieved by calculating the difference in the total volume enclosed between two images

$$\triangle V = \left\{ \sum_i^M \sum_j^N t(x_i, y_i)(\triangle x)^2 \right\}_A - \left\{ \sum_i^M \sum_j^N t(x_i, y_i)(\triangle x)^2 \right\}_B , \quad (2)$$

where t is the projected thickness of water, i and j are discrete indices of the $M \times N$ pixels in a Cartesian grid, and $\triangle x$ is the pixel size.[5]

For absorption-contrast radiographs, t can easily be determined by rearranging the Beer–Lambert law as $t = -1/\mu_w \log(I_E)$, where I_E is the normalized intensity at the exit surface and μ_w is the attenuation coefficient of water for a monochromatic source. However, when using PBI to visualize the airways, the effects of propagation-based phase contrast must first be removed for volumetric analysis. Paganin *et al.*[24] showed that the projected thickness of a single-material object can be determined from a single PBI image using

$$T(x, y) = -\frac{1}{\mu_\omega} \log \left(\mathbf{F}^{-1} \left\{ \frac{\mathbf{F}[I_R(x, y, z = \Delta)]}{1 + (\delta_\omega \Delta / \mu_\omega) |\mathbf{k}_\perp|^2} \right\} \right), \quad (3)$$

where I_R is the normalized intensity at the detector, Δ is the object-to-detector propagation distance, δ_w is the refractive index decrement of water, and $\mathbf{k}_\perp$ represents the spatial frequency components corresponding to (x,y).

The total volume in chest images includes contributions from all materials, including bone, soft tissue, and water. Kitchen *et al.*[5] were able to accurately calculate the total change in lung air volume by ensuring the ROI chosen enclosed the entire thoracic cage such that the volume of materials other than water cancelled out when applying Eq. (2) (a proof is provided in the Appendix). They also performed a quadrant analysis whereby the chest was partitioned into four regions and the lung air volume enclosed in each was measured. This method has been utilized in several research

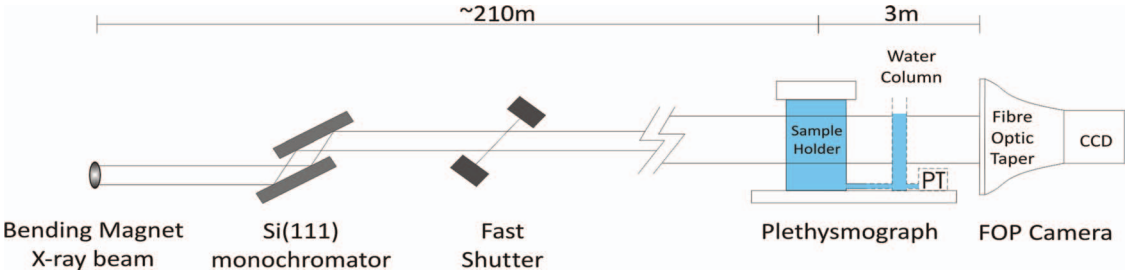

FIG. 1. A schematic of the PBI system used to acquire chest images of rabbit pups. Note that the water column is not within the path of the x-ray beam and PT = pressure transducer.

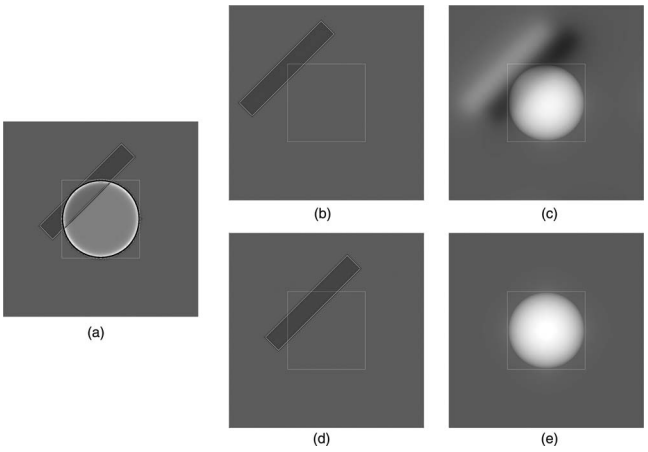

FIG. 2. Simulated images to demonstrate the necessity of aligning bone for measuring regional lung air volume. (a) A PBI image enclosing two objects, namely, a sphere (simulating an air bubble) and a cuboid (simulating bone tissue), projected onto one another and immersed in water. In (b) and (d), the PBI image of only the bone (i.e., with no air bubble) is, respectively, misaligned and aligned with that in (a). Each image underwent phase retrieval and subtraction was performed between (a) and (b) and (a) and (d) to yield the change in projected thickness at each pixel. The results are shown in (c) and (d), respectively. The change in air volume due to the sphere was calculated from these subtracted images using the entire field-of-view and using just the small ROI within the white border to demonstrate the need for image registration for regional volume measurements.

studies investigating different mechanical ventilation strategies for preterm infants, using a rabbit pup model, providing insight into the homogeneity of lung aeration at birth.[25,26] Although the bone attenuation will vary in each of the four regions, only small bone fragments will move in or out of the regions between frames, hence their movement will have little effect on the calculated lung air volumes. However, for more localized regions of the lungs, movement induced variation in the projected volume of bone can lead to large errors in lung air volumes. Our TS method corrects for this by first segmenting out the thoracic cage from the images.

To illustrate the benefit of segmenting out the thoracic cage, consider the PBI image consisting of two objects shown in Fig. 2(a). The spherical object can be considered as a pocket of air within lung tissue and the rectangular object as a bone. The PBI image was produced by generating a 1000 × 1000 pixel projected thickness map of the objects and using the angular spectrum formulation of scalar diffraction integrals to propagate the absorption-based image forward by 3 m with the pixel size set at 4.05 μm.[24] The δ and μ assigned for bone were 7.145×10^{-7} and 461.1 m^{-1}, respectively. For tissue, δ and μ were equal to 3.991×10^{-7} and 13.983 m^{-1}, respectively. These values were calculated from the NIST database[27] corresponding to a 24 keV source. Using the nonaerated PBI image shown in Fig. 2(b), the volume of the lung was determined using Eqs. (2) and (3). The change in projected thicknesses between the two images is shown in Fig. 2(c) and although the bones are not aligned, as long as they are both entirely within the field-of-view of the images, they will cancel each other out when the total change in volume is calculated, thus accurately yielding the air volume. The volume of the sphere was calculated as 2.218 μl in comparison to the known volume of 2.226 μl. This demonstrates that the technique developed by Kitchen *et al.*[5] is accurate in measuring the total lung air volume without needing to align the bones. However, when the field-of-view was restricted to a smaller region, as shown by the white border in Figs. 2(a)–2(e), the volume of bone within the smaller region in Figs. 2(a) and 2(b) is different. The change in volume calculated between these two subimages gave an air volume of just 1.688 μl—approximately a 32% error. By aligning the bones prior to subtraction [Fig. 2(d)], their effect can be eliminated when the images are subtracted, as shown in Fig. 2(e). The calculated lung air volume then was 2.186 μl—approximately only a 2% error.

II. MATERIALS AND METHODS

II.A. Image acquisition

Imaging experiments were performed in Hutch 3 of beamline 20B2 at the SPring-8 synchrotron radiation source, Japan.[28] A Si (111) double-bounce monochromator was tuned to 24 keV, which has been shown to provide optimum signal-to-noise ratio and bone/soft-tissue contrast for imaging rabbit pups on this beamline.[5] The PBI setup was adapted with the subject placed approximately 210 m downstream of the source with the detector positioned a further 3 m downstream (Fig. 1). Newborn rabbit pups were imaged as part of two experiments. The first group were imaged live at a frame rate of 3 Hz, with a respiratory cycle of 2.5 s, to study the efficacy of different ventilation strategies. Images were recorded with an exposure time of 40 ms using a high resolution detector composed of a tapered fiber optic bonded between the 4000 × 2672 pixel Hamamatsu CCD camera (C4742-95HR) and a 20 μm thick gadolinium oxysulfide ($Gd_2O_2S:Tb^+$; P43) phosphor. The effective pixel size was 16.2 μm based on the taper ratio of 1.8:1. Pups in the second group were humanely killed via anesthetic overdose prior to imaging for studying the pressure–volume characteristics of newborn lungs. These pups were imaged at a frame rate of 1 Hz, with a respiratory cycle of ~10 min, using a 25 μm thick gadolinium oxysulfide phosphor-coupled CCD camera (Hamamatsu, C4742-95HR). A tandem lens system provided an effective pixel size of 22.47 μm (2 × 2 pixel binning).

II.B. Sample preparation

All animal experiments were originally performed for studying lung aeration at birth.[26] Here, we have utilized the images recorded from those experiments for our study. All procedures involving animals were approved by the Monash University Animal Ethics Committee and the SPring-8 Animal Care and Use Committee. Pregnant New Zealand white rabbits at 31 days of gestation were anesthetized by an intravenous injection of propofol (Rapinovet; 12 mg kg^{-1} bolus, 40 mg h^{-1} infusion). Rabbit pups were delivered by caesarean section, sedated and surgically intubated. The umbilical cord was then cut and the pups were placed in

a water-filled cylindrical poly-methyl methacrylate (PMMA) container, with their heads out of the container and sealed by a rubber diaphragm surrounding their necks. A custom-made remotely controlled mechanical ventilator was connected to the endotracheal tube.[29] Ventilation began after several images were recorded of the lungs in their fluid-filled state. Rabbits and rabbit pups were humanely killed at the end of each experiment via anesthetic overdose.

II.C. Image processing

For quantitative volumetric analysis, the dark current arising from the detector was subtracted from the images, which were subsequently normalized against the incident beam intensity. This was achieved by first averaging 20 dark field images with the shutter closed and 20 flat field images with the shutter reopened and the object absent, at the end of each sequence. Nonlinear spatial distortions arising from the fiber optic camera, as a result of imperfect alignment of the fiber bundles at each end of the taper, were corrected by the use of Delaunay triangulation with bilinear interpolation.[17] Low-frequency trends were then removed to aid the cross correlation process since it is highly sensitive to large transverse gradients in the background intensity and their removal reduced the occurrence of misregistrations. These trends included: (i) the parabolic profile produced by the cylindrical container; (ii) the high energy (harmonic) x-rays reflected by the crystal monochromators creating a narrow horizontal band across the image; and (iii) the low frequency components of the air-filled lungs (which was added back when performing the lung volume analysis). To correct for the polynomial trend, a horizontal rectangular ROI below the lungs was selected along the container, averaged vertically, smoothed, then least-squares fitted with a 6th order polynomial. The polynomial curve was extruded vertically and subtracted from the images. The higher harmonic contaminants were corrected in the same manner but without polynomial fitting. The low frequency components of the aerated lungs were removed by subtracting a 200×200 pixel boxcar smoothed image of the lungs.

During the sequence acquisition the beam intensity was prone to fluctuation due, for example, to the loss and top-up of electrons in the synchrotron storage ring and thermal drifting of the monochromator crystals. This was corrected by rescaling each image to the reference frame using the average intensity in a region away from the moving pup. The Interactive Data Language (IDL 7.1) was used to run all custom-developed image processing algorithms on a PC using an Intel®Core™2 Duo, 3.32 GHZ CPU with 4 GB of RAM.

II.D. Image registration

A suitable fetal image with no lung aeration was selected as the reference image, which was then registered to each aerated image. This was achieved in two steps, where images were corrected first for global then local distortions. Each image pair was initially globally aligned to correct for the movement relating to the pup floating in the container. Kitchen *et al.*[5] achieved this by tracking the movement of a single vertebras using Eq. (1). Here, we have extended this approach to tracking multiple vertebras as it was found that each moved slightly independently to one another. The sizes and coordinates of the kernels enclosing each vertebras in the fetal (non-aerated) image were specified by the user. The corresponding search areas were automatically centerd at the same coordinates and enlarged by 10%. Each pair of control points were determined using Eq. (1), which were then replicated horizontally to both edges of the image, allowing the images to be interpolated in their entirety. This aligned the vertebral column of the two images and transformed the chest accordingly. This enabled the coordinates of regions where the ribs articulated with the vertebra (VR points) to be fixed between images for application of the localized distortion correction algorithm (described next).

The thoracic cavity was then partitioned into three regions: left/right lungs and the vertebral column. A series of 64×64 pixel kernels were selected at a sample rate of 32 pixels for the left and right lungs and correlated with their corresponding 128×128 pixel search areas. This corrected for localized movements associated with the expansion of the thoracic cage. This particular kernel size was chosen as it was sufficiently large to enclose a small segment of at most a single rib as each moves independently. The search area size was chosen to account for the largest likely rib displacements. These sizes can easily be modified if the parameters of the imaging system, such as magnification and pixel size, are changed.

The control points determined using Eq. (1) underwent a filtration process to remove unrealistic vectors. Control points were kept if all three of the following criteria were met: (i) the CC value was above a given threshold value;[30] (ii) the absolute difference between the angle of the shift vector and average angle of the adjacent shift vectors was less than 20°; and (iii) the absolute difference between the magnitude of the shift vector and average magnitude of the adjacent shift vectors was less than 81 μm (5 pixels). Image noise causes noise to also be present in the CC. A threshold value was applied to ensure matched regions with CC values significantly greater than that returned by a purely noisy region was accepted only. This threshold value was chosen to equal the average CC value returned when a pair of water-only 64×64 pixel ROIs chosen outside the rabbit, but within the container, were correlated. The angle 20° and magnitude 81 μm were selected based on a trial and error approach. These values were found to optimize the ratio of realistic to unrealistic shift vectors for chest images with various degrees of movement, yielding comparatively smooth transformations. The left and right lungs were transformed using the filtered control points and recombined together with the vertebral column to construct the registered image. To minimize the computation time required to perform temporal subtraction and phase retrieval, the region outside the chest, which includes the forelimbs, were masked out.

II.E. Image analysis

For the lung volume calculations, only the attenuation coefficient (μ_w) and refractive index decrement (δ_w) of

water were required. The latter was calculated from the NIST database[27] to be 3.99×10^{-7} (24 keV), while the former was calibrated by isolating a large section of 20 PBI images that contained water only. The lack of phase-induced intensity variations within these sections makes phase retrieval unnecessary, which allows them to be approximated as absorption-based images. The inner and outer diameter of the tube was measured to be 32.0 ± 0.1 and 39.0 ± 0.1 mm, respectively. Using the Beer–Lambert attenuation law, the attenuation coefficient of PMMA ($\mu_{\mathrm{PMMA}} = 48.91\ \mathrm{m}^{-1}$) obtained from the NIST database[27] and its thickness (7 mm), the attenuation signal of the tube was removed. μ_w was then measured to be $54.64 \pm 0.01\ \mathrm{m}^{-1}$ using the Beer–Lambert law. The absolute uncertainty of the net water volume was then determined by measuring the standard deviation (σ) of the volume difference in a water-only ROI between the reference and set of 2252 aerated images against the ROI size (N $\times$ M pixels). The points were fitted with a rational exponent function ($3.543 \times 10^{-7} \times [\mathrm{N} \times \mathrm{M}]^{3/4} + 3.654 \times 10^{-6}$) from which we can calculate σ for any sized ROI.

III. RESULTS AND ANALYSIS

III.A. Chest segmentation

We successfully tested our TS algorithm on several sets of PBI images of rabbit pup chests during mechanical ventilation. A fetal image with fluid-filled lungs and no lung aeration (reference image) was chosen and temporally subtracted from each image recorded during ventilation. Figure 3(a) shows the fluid-filled lungs of the reference image from one such dataset. The remaining sequence of images, Figs. 3(b)–3(e), shows the chest in motion during one respiratory cycle. The speckle pattern seen in the aerated chest images is created by x-rays converging as a consequence of the alveoli mimicking aberrated compound refractive lenses.[6] As a consequence of utilizing a nonaerated image, the calculated volume difference is approximately equal to the total lung air volume in the aerated image; thus, we can measure absolute rather than relative lung air volumes. Furthermore, the lack of speckles in the nonaerated image means the kernel can treat the speckles in the search area as high frequency noise, against which CC is robust, hence only the bone is tracked.

Figure 4(a) shows the direct subtraction of Figs. 3(a) and 3(c). Due to the expansion of the thoracic cage as the lung fills with air and movement of the pup, the bones do not exactly overlap and therefore bone artifacts appear in the subtracted image. The images were then registered to correct for global movement. Here ends the similarity between our technique and that of Kitchen *et al.*[5] While in both cases the vertebral column is aligned, our technique proceeds to align the ribs, thus forming a fully registered image. Images whose vertebral column is only aligned are denoted as unregistered images. Figure 4(b) displays the images subtracted after global correction. This shows the vertebral column aligned accurately, while each rib appears to rotate about the side of the connected vertebra. This highlights our assumption made earlier on the VR points being fixed to be a good approximation when aligning the ribs.

Local translation vectors were next derived for each lung to correct for the rib movement, and screened for unrealistic vectors. Approximately one tenth of the resultant translation vectors are displayed in Fig. 4(c) for clarity. The zero magnitude translation vectors at the VR points are not visible. A histogram showing the distribution of the magnitude of the resultant translation vectors is presented in Fig. 4(d). This shows a majority of the magnitudes are realistic since they are approximately consistent with the extent of displacement of the ribs. A small minority of unrealistic translational vectors remain. Although we could alter our selection

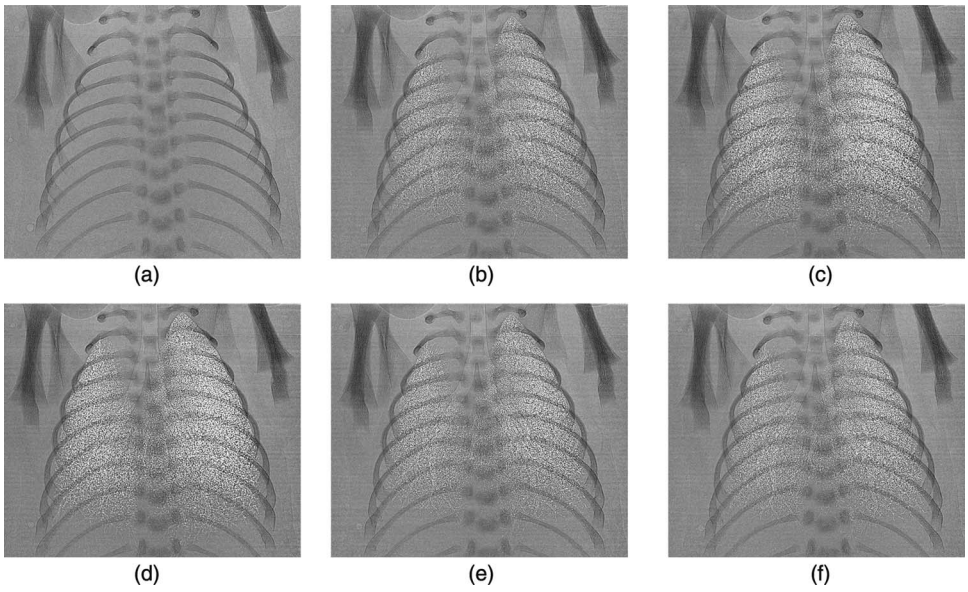

FIG. 3. A series of 24 $\times$21 mm^2 PBI chest images of a newborn rabbit pup recorded at 3 Hz in a (a) fluid-filled fetal state and (b)–(f) over one respiratory cycle, beginning midinspiration.

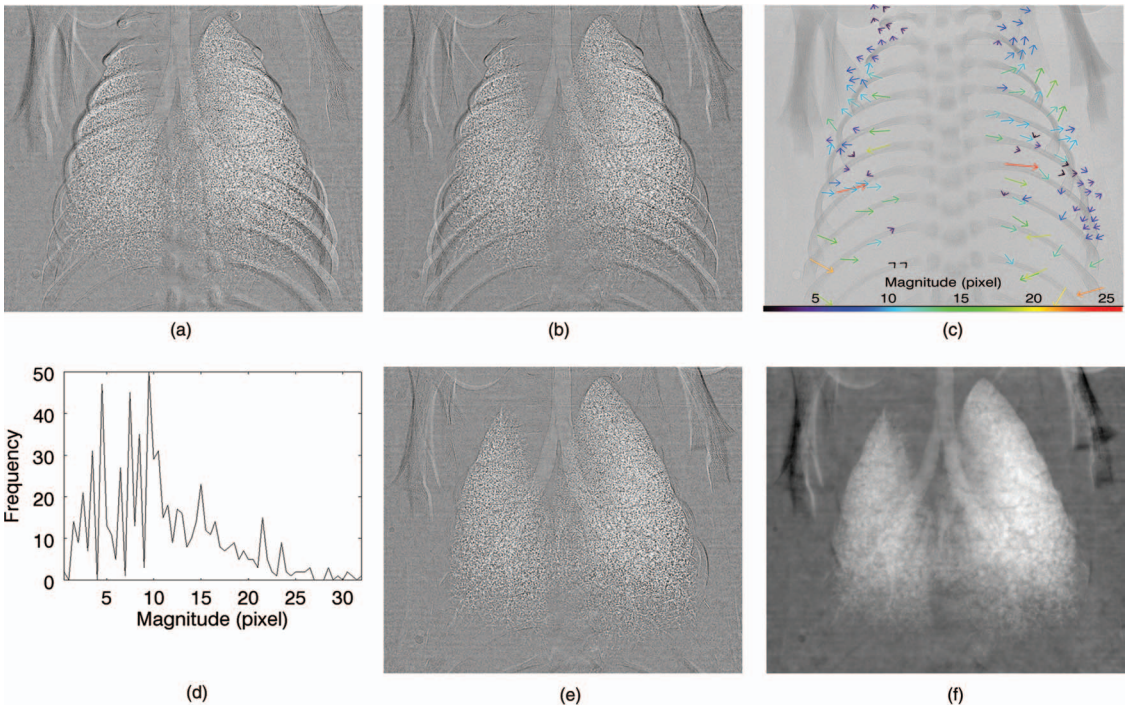

FIG. 4. Temporal subtraction. (a) The direct subtraction of the nonaerated [Fig. 3(a)] and an aerated [Fig. 3(c)] image shows the relative movement of the bony structures during image acquisition. (b) Subtraction after alignment of the vertebras in the nonaerated image with that of the aerated. (c) After correlating the entire thoracic cage, the control point pairs are represented by translational vectors (~one tenth of the vectors are shown), which enabled the nonaerated image to be transformed using bilinear interpolation. (d) A histogram showing the distribution of the magnitude of the translational vectors (the zero magnitude translation vectors have been suppressed). (e) Subtraction of the transformed image from that of the aerated image leaving only the signal due to the air (plus artifacts). (f) To perform lung volume analysis, the registered images underwent phase retrieval before subtraction, yielding the change in projected thickness at each pixel. Image size: 24×21 mm^2.

criteria to become more stringent, too many realistic translational vectors would also be filtered out, thereby adversely affecting accuracy of the alignment.

Using the control points, the reference image was transformed and subtracted from the aerated image, as shown in Fig. 4(e). Only small misalignment errors can be seen as faint artifacts predominantly along the outer borders of the chest. Since alignment was restricted to within the chest, strong artifacts are visible outside the chest. The total time taken to perform the TS was approximately 7 s on the aforementioned PC (see Sec. II.C). Figure 4(f) reveals the subtracted phase-retrieved images yielding the projected thickness of air. Note that these images underwent phase retrieval before subtraction due to the nonlinear dependence between the intensity and projected material thickness. A ROI of any size or shape could then be chosen from Fig. 4(f) to calculate the lung air volume enclosed within it.

III.B. Lung volume calculations

Figure 5(a) shows total lung air volumes calculated using the registered and unregistered reference images during mechanical ventilation of the pup. That is, we compared our technique to that of Kitchen *et al.*[5] Both techniques return almost identical total lung air volumes with the small discrepancies attributed to the rescaling of the fluid-filled nonaerated image when it was registered. The small discrepancies are well within the uncertainties of both techniques, demonstrating there is negligible detrimental effect of image registration on altering the total volume of the nonaerated image.

We proceeded to compare the ability of the two techniques to measure lung air volume on a pixel-by-pixel basis. For 1000 sequential PBI images of the same pup in Fig. 4, the lung air volume was computed at each pixel using the two techniques. The percentage difference in the calculated lung air volume between the two techniques was calculated at each pixel for the 1000 images. A histogram was computed, as shown in Fig. 5(b), which shows the distribution of the percentage difference in the calculated lung air volume averaged over all of the images. The shaded region in Fig. 5(b) shows that on average 16% of pixels within the lungs have a volume difference greater than 20%, and given that the fractional uncertainty of the measured change in lung air volume in each pixel is only ~1%, these differences are significant. The majority of these differences occurred around where the bones were not aligned, as evidenced in Figs. 5(c)–5(d) . These numbers show that the bones have a detrimental effect when performing regional lung air volume analysis and our technique is able to effectively remove the bones to accurately measure the lung air volume on a pixel-by-pixel basis.

A set of PBI chest images attained from the second group (slow inflation rates; ~10 min) was used to determine the percentage of regional lung aeration over time. Each aerated image was aligned to the first (nonaerated) image of the

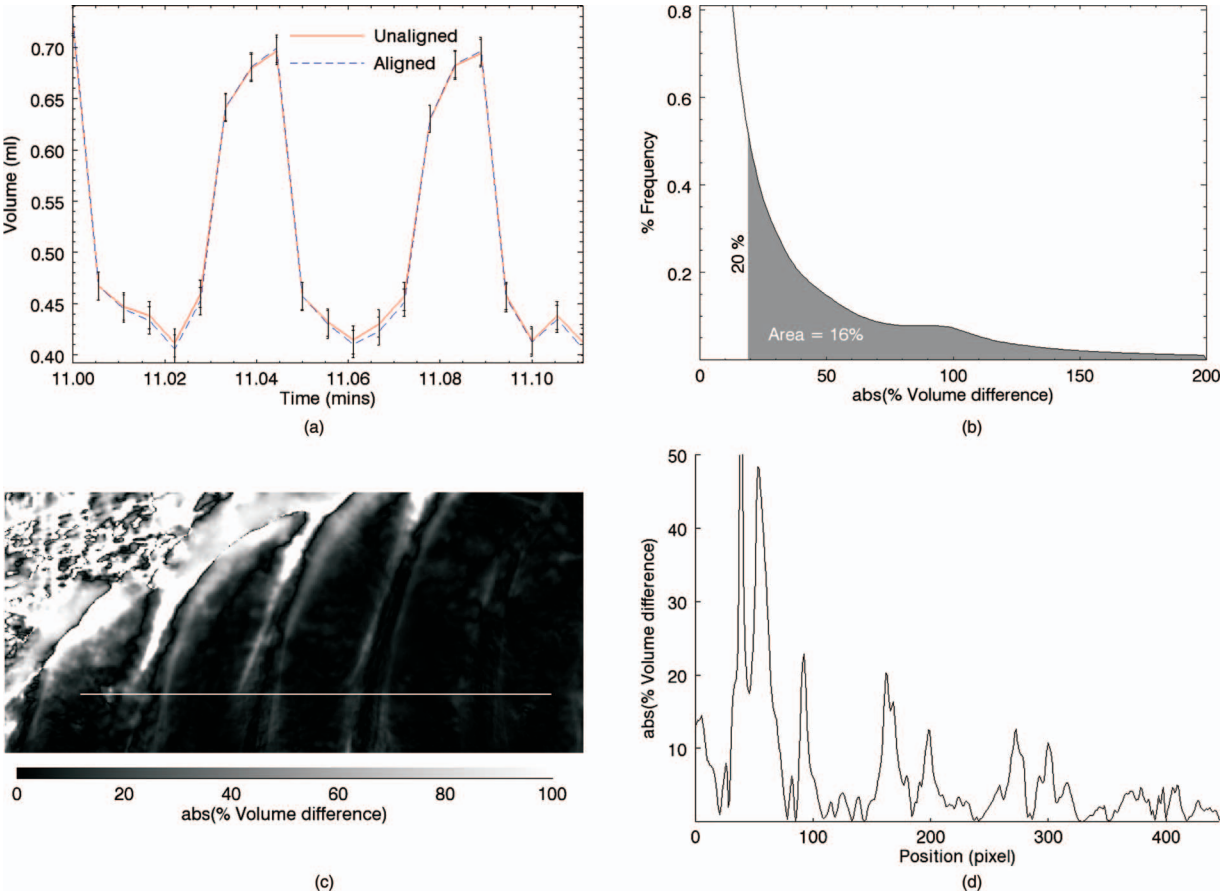

FIG. 5. Lung air volume analysis. (a) The total lung air volume was determined over several respiratory cycles beginning at $t = 11$ min, after initiation of mechanical ventilation, using the misaligned (unregistered) and aligned (registered) nonaerated images. (b) A histogram, averaged over 1000 aerated images, representing the absolute % volume difference in the calculated pixel-by-pixel lung air volume using misaligned and aligned nonaerated images. The shaded area under the plot shows the percentage of pixels with a volume difference greater than 20%. (c) An image of half a lung whose values represent the percentage difference of the lung air volume calculated between the two techniques. (d) A plot of the line profile indicated by the thick white horizontal line in (c).

sequence and underwent phase retrieval. The phase retrieved images were stacked to determine the time when each pixel within the lungs reached its maximum air volume. Figure 6 shows maps of the time taken for each region of the lungs to reach 10%, 50%, and 80% of its maximum air volume, on a pixel-by-pixel basis. We see that the major airways aerated first, as expected, followed by an otherwise relatively uniform aeration up to 10% of maximum volume [Fig. 6(a)]. However, the left lung (left side of image) then aerated more quickly in comparison to the right lung [Fig. 6(b)]. The peripheral regions of the lungs are also seen to more slowly ventilate during the latter stages of the inspiratory period. At the end of inspiration, the lungs asymptoted toward their maximum air volume more uniformly as the applied airway pressure also

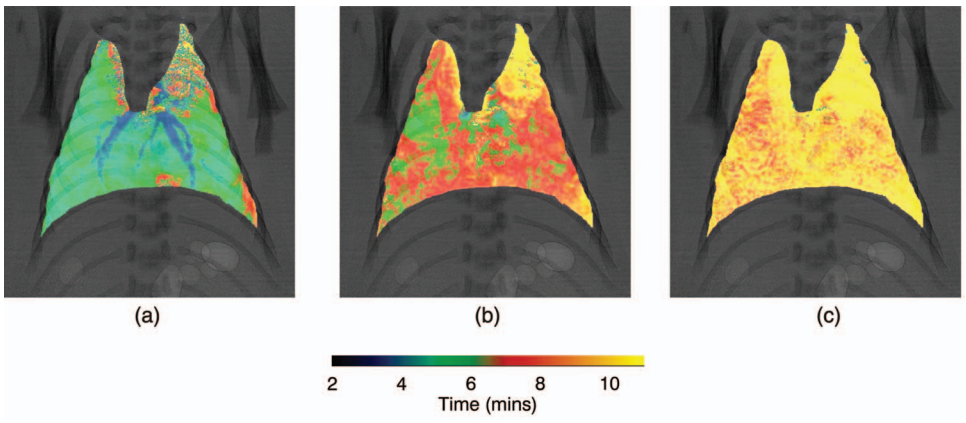

FIG. 6. Nonuniform lung aeration. A series of maps were produced showing the time taken for each pixel of the lung to reach (a) 10%, (b) 50%, and (c) 80% of their maximum air volume. Image size: 24×21 mm^2.

reached its plateau [Fig. 6(c)]. The combined panels in Fig. 6 show that the time constant of aeration is highly localized.

IV. DISCUSSION

This study demonstrates that the technique for measuring lung air volume, developed by Kitchen *et al.*,[5] can be extended to more accurately measure regional lung air volumes using TS. The image registration method adapted here has been able to accurately align PBI chest images with minimal computational cost, primarily by exploiting the use of fast Fourier transform-based CC. Other similarity measures were investigated, namely, mutual information and sums of absolute differences,[14] and the resultant subtracted images at best showed a marginal improvement, based on the visual inspection of artifacts, coinciding with a large increase in computation time. Polynomial interpolation was also considered as an alternative to bilinear interpolation since it has the ability to produce a smooth transformation; however, the complexity in the motion of the chest requires a higher order polynomial that can introduce large and unwanted oscillations around the edges of the image by the Runge phenomenon.[31]

Figure 6 shows the distribution of gas is often inhomogeneous across the lung. Hence, a regional mapping of lung aeration can reveal abnormally ventilated regions of the lung that would otherwise be undetected in global pulmonary tests. The ability to study the homogeneity of lung aeration can be beneficial in animal research studies. For example, greater understanding can be gained into lung related diseases and studying which mechanical ventilation strategies are most likely to reduce ventilator-induced lung injury (for example, for preterm infant resuscitation[26]). Our technique can also gain insight into the crucial but transient period of achieving lung aeration from birth. High-powered laboratory-based x-ray sources are being developed that enable PBI, and therefore our technique, to be performed in clinics. This presents various potential medical applications such as diagnosing respiratory related diseases earlier and with greater precision than conventional x-ray imaging and global pulmonary tests.

Compared to absorption-based x-ray imaging, PBI of the chest can provide additional structural information regarding the morphology of the conducting zone that contains the trachea, bronchi, and bronchioles, and the respiratory zone which includes the alveoli.[32] However, the signal intensity from the bone is weakened by that of the alveolar speckles. Consequently, during image registration the kernels selected in those parts of the lungs either weakly correlated, or misregistered, to regions enclosing strongly speckled intensity. This resulted in a moderate portion of translation vectors rejected in the central areas of the lungs, as shown in Fig. 4(c) by the lack of translation vectors. Despite this, the movement of the medial segment of the ribs during breathing is closely restricted to a rigid type transformation. This can be adequately accounted for by the piecewise linear interpolation between the zero magnitude VR points and their laterally closest translation vector.

The accuracy of the assumption that the medial segment of the ribs undergoes a rigid type transformation, and therefore that of alignment, depended on the amount of differential movement of the chest. A measurable indicator of the degree of motion was the volume change (the difference in volume between an aerated and nonaerated lung). It was found on average at a volume change of 0.60 ml the alignment was quite accurate but gradually deteriorated beyond this volume as the movement of the thoracic cage became overly complex (see the supplementary material for online movie).[37] Given that the average weight of a rabbit pup is 30 g, the maximum volume change per unit mass of 20 ml/kg is considered to be a large volume change.[33] Therefore, this technique could be applied to measure a range of lung air volumes in patients.

A nonaerated reference image may not always be available or possible to obtain in some studies. Alternatively, an aerated PBI chest image could be used as a reference image. While this will instead provide relative volumetric measurements, which still carries much important respiratory information, a more problematic issue is that cross-correlating ROIs that have speckles present in both is likely to increase the prevalence of misregistrations as the speckles weaken the signal intensity of the bone. Moreover, the speckles may correlate more strongly with each other than the bones themselves. Consequently, measuring relative changes in lung air volume by using an aerated chest image as a reference image decreases the maximum volume change per unit mass that our technique can measure.

Regardless of whether the reference image is an aerated or nonaerated chest image, the maximum measurable volume change could be increased either through modifying the algorithm or image acquisition process. More translation vectors could be retained by correcting rather than rejecting them. These corrections could be made based on preserving the continuity and smoothness of the transformation (see, e.g., Ref. 34). We also attempted using a smaller sized kernel to better handle the localized lung movement. This increased the number of degrees of freedom, but the structural information it enclosed was less unique and became more prone to misregistrations. Shortening the propagation distance to reduce or remove the phase contrast could improve the bone contrast relative to the speckle contrast to reduce the occurrence of misregistrations. If the reference image was an aerated PBI chest image, then it could be chosen to be the image with the least lung aeration. We have also discovered that the degree of chest wall movement is dependent on the angle between the vertebral column and the horizontal axis along the sagittal plane. We are currently attempting to optimize this orientation to enable accurate alignment at volume changes up to 40 ml/kg.

The total lung air volume was expected to remain unchanged before and after temporal subtraction considering that all the anatomical structure remained within the detector field-of-view. Due to the nonconservation of the total intensity when performing a nonrigid type transformation, there would inevitably be a small deviation. To ascertain the extent at which the nonconserving volume contributes regionally, the calculated lung air volume using temporal subtraction could be compared with that using other bone removal techniques. One example is the technique developed by Kitchen *et al.*[35]

that utilizes a Laue crystal to split the x-ray beam to create two unique images. These have been used to segment chest images to enable isolation of bony anatomy and soft tissue and regional lung volume measurement. Although that technique does not require anatomical registration, it is experimentally more challenging, the image reconstruction is also more time consuming and somewhat susceptible to low frequency noise. Nonetheless, it presents as an ideal technique with which to compare our calculated regional lung air volumes.

Throughout, we have employed a fixed sized ROI to measure lung aeration. To correctly assess regional volumes, the expansion and deflation of the lungs should be taken into account. Christensen *et al.*[36] showed that lungs do not expand or relax uniformly but in a local manner. Fouras *et al.*[15] developed a particle image velocimetry-based algorithm that is able to measure regional expansion of the lungs by tracking the motion of the lung-induced speckles. Thus, we will look to adapt the work of Fouras *et al.*[15] into our method to measure regional air volume of the entire lung by deforming the ROI in accordance with the movement of the speckles.

V. CONCLUSIONS

Accurately measuring the heterogeneity of lung aeration is likely to be highly beneficial to studying and treating child and adult lung disease and for optimizing mechanical ventilation strategies for preterm infants. Herein, a temporal subtraction algorithm was developed to remove the bony anatomy from two-dimensional propagation-based phase contrast x-ray images of the chest to isolate the lungs. Using a single image phase retrieval algorithm the change in air volumes between localized regions of the lung, down to the micron scale pixel size, could be measured. By comparing the total lung air volume measured using a registered and unregistered nonaerated image, we found that the variability in the total intensity introduced in the nonaerated chest image of preterm rabbit pups after image registration is small compared to the uncertainty in our measured change in lung air volume. In analyzing the lung air volume regionally, we showed a significant improvement, compared to images that were not registered, primarily in areas where the bones were poorly aligned. Therefore, we have demonstrated that our technique can isolate the lungs and provide high spatiotemporal resolution measures of lung aeration, without the requirement of contrast agents.

ACKNOWLEDGMENTS

The authors would like to thank Dr. David Paganin, Dr. Karen Siu, and Dr. Imants Svalbe for insightful discussions, and to Kentaro Uesugi for assistance with the experiments. A.F.T.L. acknowledges the support of an Australian Postgraduate Award. A.F., S.B.H., and M.J.K. acknowledge funding from the Australian Research Council (ARC; Grant Nos. DP110101941 and DP110101498). M.J.K. is an ARC Australian Research Fellow. S.B.H. is a NHMRC Principal Research Fellow. This research was partially funded by the Victorian Government's Operational Infrastructure Support Program. The authors acknowledge travel funding provided by the International Synchrotron Access Program managed by the Australian Synchrotron and funded by the Australian Government.

APPENDIX: MEASURING THE CHANGE IN VOLUME OF A SINGLE MATERIAL FROM A HETEROGENEOUS OBJECT

Consider a multimaterial object where the volume of only one of the materials is changing over time. If a sequence of absorption-based images were recorded of that object, the change in volume of that material can be measured between the recorded images. Here, we will demonstrate this by first considering two $M \times N$ pixel absorption-based images (I_1, I_2) at the exit surface plane of the object at time points 1 and 2. The intensity can be related to the projected thickness of the materials given by Beer–Lambert's law,

$$I(x, y) = \exp[-\textstyle\sum_{\mathrm{m}} \mu_{\mathrm{m}}(x_i, y_j) t_m(x_i, y_j)], \tag{A1}$$

where μ_m and t_m are the attenuation coefficient and projected thickness of material m, respectively. i and j are discrete indices of the $M \times N$ pixels in a Cartesian grid.

The projected thickness (t_w) corresponding to the material with a changing volume can be isolated from Eq. (A1) by assuming the other materials are also made entirely of that material to give

$$t_w(x_i, y_i) + \sum_m t'_m(x_i, y_i) = -\frac{1}{\mu_w} \log_e[I(x_i, y_i)], \tag{A2}$$

where $t'_m = \mu_w / \mu_m t_m$, which shows the projected thickness of each material rescaled to separate μ from t. t_w can be isolated by taking the difference in the projected thicknesses of I_1 and I_2, and summing over (x_i, y_j) to give

$$\begin{aligned} \triangle t_w &= \sum_i^M \sum_j^N [t_{w,1}(x_i, y_i) - t_{w,2}(x_i, y_i)] \\ &= \sum_i^M \sum_j^N \left\{ \frac{1}{\mu_w} [log_e[I_2(x_i, y_i)] - log_e[I_1(x_i, y_i)]] \right\}. \end{aligned} \tag{A3}$$

Since the total projected thickness of the other materials remain constant, the second term on the left-hand side of Eq. (A2) cancel out, thus correctly giving the change in the total projected thickness of material w. By multiplying Eq. (A3) with the pixel area, we arrive at Eq. (2). For our work, the changing volume we are measuring is air, although it cannot be directly measured due to its low attenuating strength. Instead, the lungs are immersed in a tube of water where the volume of water displaced during breathing is equivalent to that of air.

In our work, we recorded PBI images, thus the single-image phase retrieval algorithm is applied before using the steps above. This algorithm convolves the PBI image with a radially dependant low-pass filter function to obtain the absorption-based image, effectively smoothing out the phase induced intensity variations. As a consequence of using

Eq. (3) on an inhomogeneous object such as the chest, materials with a ratio μ/δ different to that of the material of interest will be over/undersmoothed. The degree of over/undersmoothing varies with lung aeration. Despite this, the work done by Kitchen *et al.*[5] shows that the change in lung air volume calculated using their technique correlates well with that measured from a plethysmograph for numerous preterm rabbit pups over a large range of lung air volumes. This demonstrates the error introduced, from over/undersmoothed materials, into the measured change in lung air volume is small relative to its uncertainty.

[a]Electronic mail: andrew.leong@monash.edu.

[1]A. Fouras, M. J. Kitchen, S. Dubsky, R. A. Lewis, S. B. Hooper, and K. Hourigan, "The past, present, and future of x-ray technology for in vivo imaging of function and form," J. Appl. Phys. **105**, 102009 (2009).

[2]S. D. Qanadli, E. Orvoen-Frija, P. Lacombe, R. Di Paola, J. Bittoun, and G. Frija, "Estimation of gas and tissue lung volumes by MRI: Functional approach of lung imaging," J. Comput. Assist. Tomogr. **23**, 743–748 (1999).

[3]S. Monfraix, S. Bayat, L. Porra, G. Berruyer, C. Nemoz, W. Thomlinson, P. Suortti, and A. R. A. Sovijärvi, "Quantitative measurement of regional lung gas volume by synchrotron radiation computed tomography," Phys. Med. Biol. **50**, 1–11 (2005).

[4]T. J. Wellman, T. Winkler, E. L. Costa, G. Musch, R. S. Harris, J. G. Venegas, and M. F. V. Melo, "Measurement of regional specific lung volume change using respiratory-gated pet of inhaled ^{13}N-nitrogen," J. Nucl. Med. **51**, 646–653 (2010).

[5]M. J. Kitchen, R. A. Lewis, M. J. Morgan, M. J. Wallace, M. L. Siew, K. K. W. Siu, A. Habib, A. Fouras, N. Yagi, K. Uesugi, and S. B. Hooper, "Dynamic measures of regional lung air volume using phase contrast x-ray imaging," Phys. Med. Biol. **53**, 6065–6077 (2008).

[6]M. J. Kitchen, D. Paganin, R. A. Lewis, N. Yagi, K. Uesugi, and S. T. Mudie, "On the origin of speckle in x-ray phase contrast images of lung tissue," Phys. Med. Biol. **49**, 4335–4348 (2004).

[7]J. F. Adam, S. Bayat, L. Porra, H. Elleaume, F. Estve, and P. Suortti, "Quantative functional imaging and kinetic studies with high-Z contrast agents using synchrotron radiation computed tomography," Clin. Exp. Pharmacol. Physiol. **36**, 95–106 (2009).

[8]P. Vock and Z. Szucs-Farkas, "Dual energy subtraction: Principles and clinical applications," Eur. J. Radiol. **72**, 231–237 (2009).

[9]T. Ishigaki, S. Sakuma, Y. Horikawa, M. Ikeda, and H. Yamaguchi, "One-shot dual-energy subtraction imaging" Radiology **161**, 271–273 (1986).

[10]R. P. Carnibella, A. Fouras, and M. J. Kitchen, "Single-exposure dual-energy-subtraction x-ray imaging using a synchrotron source," J. Synchrotron Radiat. **19**, 954–959 (2012).

[11]S. Kakeda, K. Kamada, Y. Hatakeyama, T. Aoki, Y. Korogi, S. Katsuragawa, and K. Doi, "Effect of temporal subtraction technique on interpretation time and diagnostic accuracy of chest radiography," Am. J. Roentgenol. **187**, 1253–1259 (2006).

[12]K. Suzuki, H. Abe, H. MacMahon, and K. Doi, "Image-processing technique for suppressing ribs in chest radiographs by means of massive training artificial neural network (MTANN)," IEEE Trans. Med. Imaging **25**, 406–416 (2006).

[13]A. Kano, K. Doi, H. MacMahon, D. D. Hassell, and M. L. Giger, "Digital image subtraction of temporally sequential chest images for detection of interval change," Med. Phys. **21**, 453–461 (1994).

[14]B. Zitová and J. Flusser, "Image registration methods: A survey," Image Vision Comput. **21**, 977–1000 (2003).

[15]A. Fouras, B. J. Allison, M. J. Kitchen, S. Dubsky, J. Nguyen, K. Hourigan, K. K. W. Siu, R. A. Lewis, M. J. Wallace, and S. B. Hooper, "Altered lung motion is a sensitive indicator of regional lung disease," Ann. Biomed. Eng. **40**, 1160–1169 (2012).

[16]R. A. Jamison, A. Fouras, and R. J. Bryson-Richardson, "Cardiac-phase filtering in intracardiac particle image velocimetry," J. Biomed. Opt. **17**, 036007 (2012).

[17]M. S. Islam, R. A. Lewis, K. Uesugi, and M. J. Kitchen, "A high precision recipe for correcting images distorted by a tapered fiber optic," J. Instrum. **5**, P09008 (2010).

[18]G. E. Christensen, X. Geng, J. G. Kuhl, J. Bruss, T. J. Grabowski, I. A. Pirwani, M. W. Vannier, J. S. Allen, and H. Damasio, "Introduction to the non-rigid image registration evaluation project (NIREP)," in *Biomedical Image Registration*, Lecture Notes in Computer Science Vol. 4057, edited by J. Pluim *et al.* (Springer, Berlin Heidelberg, 2006), pp. 128–135.

[19]A. Momose, T. Takeda, Y. Itai, and K. Hirano, "Phase-contrast x-ray computed tomography for observing biological soft tissues," Nat. Med. **2**, 473–475 (1996).

[20]T. E. Gureyev, S. C. Mayo, D. E. Myers, Y. Nesterets, D. M. Paganin, A. Pogany, A. W. Stevenson, and S. W. Wilkins, "Refracting Röntgen's rays: Propagation-based x-ray phase contrast for biomedical imaging," J. Appl. Phys. **105**, 102005 (2009).

[21]S. A. Zhou and A. Brahme, "Development of phase-contrast x-ray imaging techniques and potential medical applications," Phys. Medica **24**, 129–148 (2008).

[22]S. W. Wilkins, T. E. Gureyev, D. Gao, A. Pogany, and A. W. Stevenson, "Phase-contrast imaging using polychromatic hard x-rays," Nature (London) **384**, 335–338 (1996).

[23]D. J. Vine, D. M. Paganin, K. M. Pavlov, J. Kráußlich, O. Wehrhan, I. Uschmann, and E. Förster, "Analyzer-based phase contrast imaging and phase retrieval using a rotating anode x-ray source," J. Appl. Phys. **91**, 254110 (2007).

[24]D. Paganin, S. C. Mayo, T. E. Gureyev, P. R. Miller, and S. W. Wilkins, "Simultaneous phase and amplitude extraction from a single defocused image of a homogeneous object," J. Microsc. **206**, 33–40 (2002).

[25]M. L. Siew, A. B. te Pas, M. J. Wallace, M. J. Kitchen, M. S. Islam, R. A. Lewis, A. Fouras, C. J. Morley, P. G. Davis, N. Yagi, K. Uesugi, and S. B. Hooper, "Surfactant increases the uniformity of lung aeration at birth in ventilated preterm rabbits," Pediatr. Res. **70**, 50–55 (2011).

[26]S. B. Hooper, M. J. Kitchen, M. L. L. Siew, R. A. Lewis, A. Fouras, A. B. te Pas, K. K. W. Siu, N. Yagi, K. Uesugi, and M. J. Wallace, "Imaging lung aeration and lung liquid clearance at birth using phase contrast x-ray imaging," Clin. Exp. Pharmacol. Physiol. **36**, 117–125 (2009).

[27]M. J. Berger, J. H. Hubbell, S. M. Seltzer, J. Chang, J. S. Coursey, R. Sukumar, D. S. Zucker, and K. Olsen, "XCOM: Photon cross sections database," 2010 (available URL: http://www.nist.gov/pml/data/xcom/index.cfm).

[28]S. Goto, K. Takeshita, Y. Suzuki, H. Ohashi, Y. Asano, H. Kimura, T. Matsushita, N. Yagi, M. Isshiki, H. Yamazaki, Y. Yoneda, K. Umetani, and T. Ishikawa, "Construction and commissioning of a 215-m-long beamline at SPring-8," Nucl. Instrum. Meth. A **467–468**, 682–685 (2001).

[29]M. J. Kitchen, A. Habib, A. Fouras, S. Dubsky, R. A. Lewis, M. J. Wallace, and S. B. Hooper, "A new design for high stability pressure-controlled ventilation for small animal lung imaging," J. Instrum. **5**, T02002 (2010).

[30]R. D. Keane and R. J. Adrian, "Optimization of particle image velocimeters. I. Double pulsed systems," Meas. Sci. Technol. **1**, 1202–1215 (1990).

[31]E. Süli and D. F. Mayers, *An Introduction to Numerical Analysis* (Cambridge University Press, Cambridge, 2003).

[32]M. J. Kitchen, R. A. Lewis, N. Yagi, K. Uesugi, D. Paganin, S. B. Hooper, G. Adams, S. Jureczek, J. Singh, C. R. Christensen, A. P. Hufton, C. J. Hall, K. C. Cheung, and K. M. Pavlov, "Phase contrast x-ray imaging of mice and rabbit lungs: A comparative study," Br. J. Radiol. **78**, 1018–1027 (2005).

[33]M. R. Wilson, B. V. Patel, and M. Takata, "Ventilation with clinically relevant high tidal volumes does not promote stretch-induced injury in the lungs of healthy mice," Crit. Care Med. **40**, 2850–2857 (2012).

[34]Q. Li, S. Katsuragawa, and K. Doi, "Improved contralateral subtraction images by use of elastic matching technique," Med. Phys. **27**, 1934–1942 (2000).

[35]M. J. Kitchen, D. M. Paganin, K. Uesugi, B. J. Allison, R. A. Lewis, S. B. Hooper, and K. M. Pavlov, "Phase contrast image segmentation using a laue analyser crystal," Phys. Med. Biol. **56**, 515–534 (2011).

[36]G. E. Christensen, J. H. Song, W. Lu, I. E. Naqa, and D. A. Low, "Tracking lung tissue motion and expansion/compression with inverse consistent image registration and spirometry," Med. Phys. **34**, 2155–2163 (2007).

[37]See supplementary material at http://dx.doi.org/10.1118/1.4794926 for online movie.